

Deep Depth Prior for Multi-View Stereo

Pallabi Ghosh

pallabig@cs.umd.edu

Vibhav Vineet

vibhav.vineet@microsoft.com

Larry S. Davis

lsd@umiacs.umd.edu

Abhinav Shrivastava

abhinav@cs.umd.edu

Sudipta Sinha

Sudipta.Sinha@microsoft.com

Neel Joshi

neel@microsoft.com

Abstract

It was recently shown that the structure of convolutional neural networks induces a strong prior favoring natural color images, a phenomena referred to as a deep image prior (DIP), which can be an effective regularizer in inverse problems such as image denoising, inpainting etc.

In this paper, we investigate a similar idea for depth images, which we call a deep depth prior. Specifically, given a color image and a noisy and incomplete target depth map from the same viewpoint, we optimize a randomly-initialized CNN model to reconstruct an RGB-D image where the depth channel gets restored by virtue of using the network structure as a prior. We propose using deep depth priors for refining and inpainting noisy depth maps within a multi-view stereo pipeline. We optimize the network parameters to minimize two losses – 1) a RGB-D reconstruction loss based on the noisy depth map and 2) a multi-view photoconsistency-based loss, which is computed using images from a geometrically calibrated camera from nearby viewpoints. Our quantitative and qualitative evaluation shows that our refined depth maps are more accurate and complete, and after fusion, produces dense 3D models of higher quality.

1. Introduction

Multi-view stereo [9, 15, 34] (MVS) refers to the task of computing a detailed 3D model of a stationary scene from multiple calibrated images. Several modern MVS methods first compute depth maps from several camera viewpoints using dense stereo matching on multiple sets of overlapping images [15, 34, 47] and then subsequently combines them using a depth-map fusion approach [10]. The stereo matching problem is inherently ill-posed and extensive research has been conducted to solve the problem using approximate inference and optimization techniques that employ appropriate priors and regularization [45, 5, 39, 40].

Supervised learning methods based on convolutional

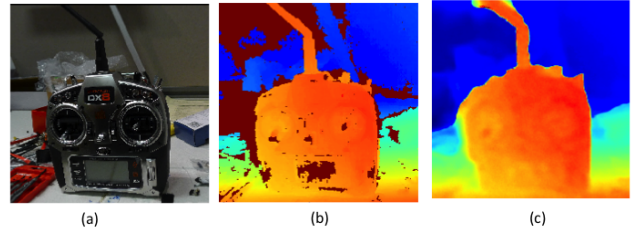


Figure 1: (a) One of the input images (b) Target depth map computed using SGM and multiple neighboring images [18] (c) The refined depth map generated using our deep depth prior (DDP) based refinement. Notice that the depth map fills the holes in (b) (shown in brown).

neural networks (CNNs) have recently shown promise in stereo, both in the binocular [48, 28, 21] and multi-view [20, 47, 19] settings. However, these supervised methods rely on vast amounts of data with ground truth disparity or depth in order to achieve proper generalization. While unsupervised learning approaches have been explored [49, 41, 30], their success appears modest compared to supervised methods.

In this work, we investigate a new approach for unsupervised stereo that is inspired by the recent work by Ulyanov et al. [42]. They demonstrated that the underlying structure of an encoder-decoder CNN induces a prior that favors natural images, a property they refer to as deep image priors (DIP). They show that the parameters of a randomly initialized encoder-decoder CNN can be optimized to map a high-dimensional noise vector to a single image. When the image is corrupted and the optimization is stopped at an appropriate point before overfitting sets in, the network outputs a remarkably noise-free image. DIP has been used as a regularizer in low-level vision tasks [42, 44, 12].

The main objective in this paper is to investigate the effectiveness of DIP-based regularization for refining and inpainting noisy and incomplete depth maps. The noisy depth maps can come from any source. In our case we used an existing efficient stereo matching algorithm [18, 16]. Similar to Ulyanov et al. [42], we also map random noise images to

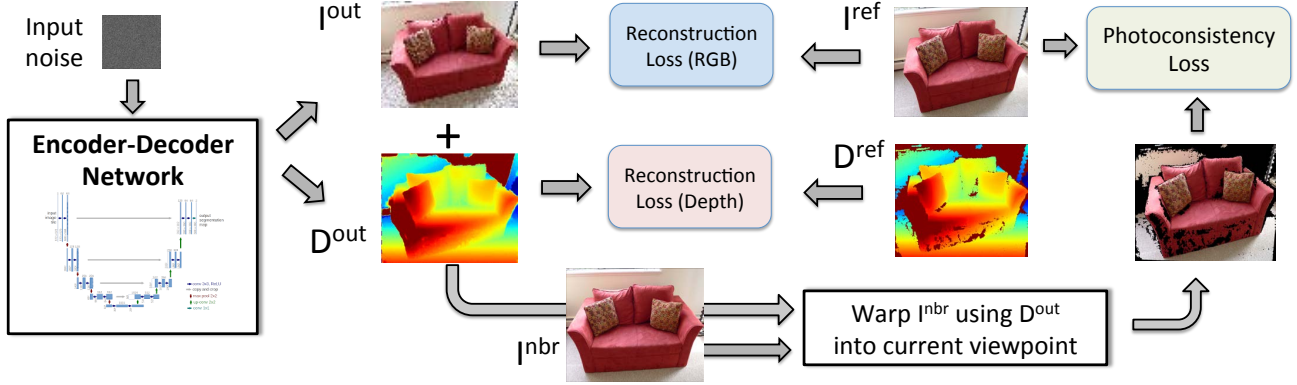


Figure 2: Overview of Deep Depth Prior (DDP): The DDP network is trained using a combination of L1 and SSIM reconstruction loss with respect to a target RGB-D image and a photo-consistency loss with respect to neighboring calibrated images. This network is used to refine a set of noisy depth maps and the refined depth maps are subsequently fused to obtain the final 3D point cloud model. I^{out} and D^{out} are the RGB and depth output of our network. I^{nbr} is the RGB at a neighboring viewpoint. I^{ref} and D^{ref} are the input RGB and depth at the current (reference) viewpoint.

target noisy depth maps using randomly initialized encoder-decoder networks- one per depth map. In our first variant, our network generates a depth map and its parameters are optimized by minimizing a depth reconstruction loss. In the other variant, our network outputs an RGB-D image and the reconstruction loss is with respect to both color and depth.

Finally, we build upon the idea of deep depth prior-based refinement and propose a formulation where the prior is combined with multi-view photoconsistency-based data terms. For this approach, we optimize the network parameters by incorporating an additional loss term, that is computed by warping the reference color image into the neighboring views using the generated depth map and then measuring the photometric discrepancy between the warped image and the original image. In this sense, our technique resembles direct methods proposed decades ago for image registration problems, which all employ some form of initialization and iterative optimization. However, instead of using handcrafted regularizers in the optimization objective, we study the use of the depth image prior as the regularizer. While the role of regularization in end-to-end trainable CNN architectures is gaining interest [25, 46], our method is quite different, because there is no training and the network parameters are optimized from scratch on new test images.

Contributions. We make the following contributions: (1) To the best of our knowledge, this is the first work to investigate deep depth priors and deep RGB-D priors, motivated by recent work on deep image priors for color images. (2) We incorporate the deep depth prior within an approach to refine a depth map given overlapping calibrated color images. In this approach, the regular reconstruction loss of the DIP network is augmented with another loss term which is based on multi-view photoconsistency with respect to the

other calibrated color images. (3) We use our depth refinement approach into a modern MVS pipeline and show that the refined depth maps lead to more accurate and complete 3D models.

2. Related Work

In this section, we broadly review existing dense stereo matching and depth refinement methods and then discuss the recent work on deep image priors and its applications.

Stereo matching. Dense stereo matching is an extensively studied topic and there has been tremendous algorithmic progress both in the binocular setting [18, 48, 28, 49, 25] as well as in the multi-view setting [34, 16, 47, 19, 10], in conjunction with advances in benchmarking [32, 14, 35, 22, 1]. Traditionally, the best performing stereo methods were based on approximate MRF inference on pixel grids [45, 5, 39], where including suitable smoothness priors was considered quite crucial. However, such methods were usually computationally expensive. Hirschmuller [18] proposed Semi-Global Matching (SGM), a method that provides a trade-off between accuracy and efficiency by approximating a 2D MRF optimization problem with several 1D optimization problems. SGM has many recent extensions [13, 2, 37, 33, 36] and also works for multiple images [16]. Region growing methods are another alternative that has also shown promise and implicitly incorporate smoothness priors [4, 34, 26, 17]

Deep Stereo. In recent years, deep models for stereo have been proposed to compute better matching costs [48, 27, 7] or to directly regress disparity or depth [28, 21, 49, 6] and also for the multi-view setting [20, 47, 19]. Earlier on, end-to-end trainable CNN models did not employ any form of explicit regularization, but recently hybrid CNN-CRF meth-

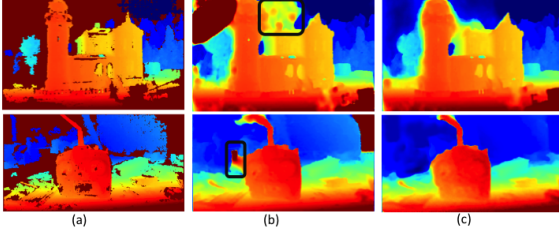


Figure 3: (a) Input depth map with holes (b) DDP on just Depth maps and (c) DDP on RGBD images. In the black box regions in (b), DDP is filling up the holes in the sky or background based on the depth from the house or radio because it has no edge information. RGBD input provides this edge information in (c).

ods have advocated using appropriate regularization based on conditional random fields (CRFs) [25, 46].

Depth Map Refinement The fast bilateral solver [3] is an optimization technique for refining disparity or depth maps. However, the objective is fully handcrafted. Knoblereiter and Pock recently proposed a refinement scheme where the regularizer in the optimization objective is trained using ground truth disparity maps [24]. Their model learns to jointly reason about image color, stereo matching confidence and disparity. Other recent disparity or depth map refinement techniques utilize trained CNN models [29].

Deep prior for color images. Ulyanov et al. proposed deep image priors [42] (DIP) and showed that the structure inherent to CNNs allowed them to act as powerful regularizers on many low-level vision problems involving natural images. Their work inspired follow-up work on diverse applications of DIP – neural inverse rendering [38], mesh reconstruction from 3D points [44], layer-based image decomposition [12]. Recently, Cheng et al. [8] pointed out important connections between DIP and Gaussian processes.

Inspired by the remarkable properties of DIP [42], we investigate using DIP-like regularizers for depth maps and propose an unsupervised depth refinement approach based on the idea. However, unlike [42], we optimize the encoder-decoder network by combining the usual reconstruction loss with a second term, the photoconsistency loss which ensures that when the reference image is warped into a neighboring view using our depth map, the discrepancy between the warped image and the original image is minimized.

3. Method

Given a RGBD image with I^{in} as RGB component and D^{in} as noisy depth component, our goal is to generate denoised and inpainted depth image D^* . We leverage recently proposed Deep Image Prior (DIP) [42] to solve this problem. Next we briefly describe the DIP approach.

3.1. Deep Image Prior

The DIP method proposed a deep network based technique for solving image denoising, restoration, inpainting problems. At the core of their method lies the idea that deep networks can serve as a prior for such inverse problems. If x is the input image, n is the input noise and x_o is the denoised output of the network f_θ , then the optimization problem of the DIP method takes the following form:

$$\theta^* = \underset{\theta}{\operatorname{argmin}} L(f_\theta(n); x), \quad x_o^* = f_{\theta^*}(n). \quad (1)$$

The task of finding the optimal neural network parameters θ^* and the optimal denoised image x_o^* is solved using standard backpropagation approach.

A simple approach to solve the depth denoising and inpainting problem would be to use a DIP like encoder-decoder architecture to improve the depth images. Here depth images would replace RGB as inputs in the original DIP framework. However this fails to fill the holes with correct depth values. Some of the visual outputs are shown in figure 3. More quantitative results are provided in Table 1b.

We hypothesize three reasons for this failure. First holes near object boundary can cause incorrect depth filling. Second depth images have more diverse values than RGB that leads to large quantization. Correctly predicting values for such large quantized space is a challenging task for the DIP network. Finally absolute error for far objects may dominate the DIP optimization over important near by objects.

3.2. Deep Depth Prior

In this work, we propose Deep Depth Prior (DDP) approach that includes three new losses to solve the issues discussed above. Our approach is built on top of the inpainting task in [42] where we create a mask for the holes in the depth map and calculate the loss over the non-masked regions.

Preliminary. To solve the issue of absolute error for far objects dominating the DIP optimizer, inverted depth or disparity images are used. We also add a constant value to depth image that reduces the ratio between the maximum and minimum depth values. Further, masking of all far away objects beyond a certain depth is performed by clipping to a predefined maximum depth value. We also clip depth to a minimum value so that the maximum disparity value does not go to infinity.

Let D^{out} be the desired depth output from our network and let f_θ denote this generator network. Input to the network is noise n^{in} and the input depth map is inverted to get z^{in} as the noisy disparity map. Let us represent the output from the network as z^{out} where $z^{out} = f_\theta(n^{in}; z^{in})$. On convergence, optimal D^* is obtained by inverting z^* .

We use three different losses to optimize our network. Total loss is:

$$L^{total} = \gamma_1 L^{disp} + \gamma_2 L^{RGB} + (1 - \gamma_1 - \gamma_2) L^{warp}. \quad (2)$$

We next describe these three losses in detail.

Disparity-based loss L^{disp} . The simplest technique to obtain z^* is to optimize only on disparity. The disparity based loss L^{disp} is a weighted combination of Mean Absolute Error (MAE) or L^1 loss and Structural Similarity metric (SSIM) or L^{ss} loss [43], and takes the following form:

$$L^{disp} = \lambda_z L^1(z^{in}, z^{out}) + (1 - \lambda_z) L^{ss}(z^{in}, z^{out}). \quad (3)$$

We use L^1 loss instead of Mean Squared Error (L^2) loss to remove the effect of very high valued noise having a major effect on the optimization. It takes the form as $L^1(z^{in}, z^{out}) = |z^{in} - z^{out}|$.

The structural similarity L^{ss} loss measures similarity between the input z^{in} and reconstructed disparity map z^{out} . Here similarity is defined at the block level where each block size is 11x11. It provides consistency at the region level. The loss (L^{ss}) takes the following form $L^{ss} = 1 - SSIM(z^{in}, z^{out})$. Details about the $SSIM$ function are provided in the supplementary material.

RGB-based loss L^{RGB} . We observed that under certain situation the disparity based loss blurs the edges in the final generated depth map. This happens when there is a hole in the depth map near an object boundary. The generator network produces depth map that is a fused version of depths of different object appearing around the hole.

For example, consider regions belonging to sky in top row of Figure 3. Due to homogeneous nature of the sky pixels, standard disparity/depth estimation methods fail to produce any disparity/depth for such regions. However, pixels corresponding to house region have depth values. When the image is passed to a DIP generator, the edge between the house and the sky gets blurred because the network is trying to fill up the space without any additional knowledge e.g., boundary information. It just bases its decision on homogeneity of space to fill up the incomplete regions as seen in the top row of Figure 3(b) in the red box region.

To solve this problem we also pass the color RGB image along with the disparity image. The encoder-decoder based DDP architecture is now trained on the 4 channel RGBD information. Weights of the network are updated not only on the masked disparity map but also on the full RGB image. This helps the network to leverage the object boundary information in the RGB image to fill the holes in the disparity (and so in depth) image. This important edge information provided to the network helps to generate crisp depth images as seen in the Fig. 3(c).

Let I^{out} be the output corresponding to input data I^{in} using the noise n^{in} and generator model f_θ . It takes the form as $I^{out} = f_\theta(n^{in}, I^{in})$.

The Loss L^{RGB} is also a weighted combination of L^1 and $SSIM$ losses, and is defined as:

$$L^{RGB} = \lambda_I L^1(I^{in}, I^{out}) + (1 - \lambda_I) L^{ss}(I^{in}, I^{out}). \quad (4)$$

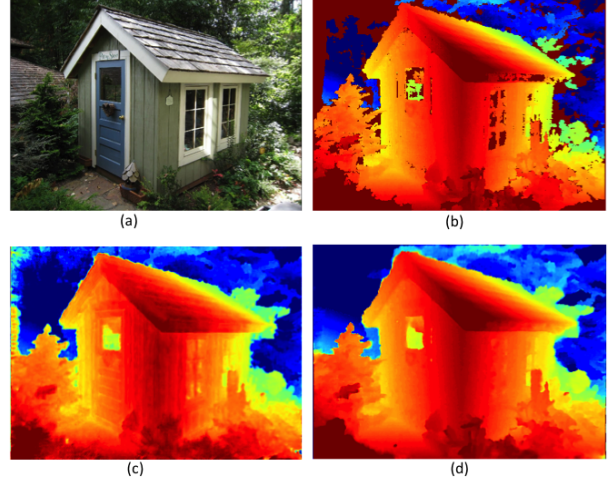


Figure 4: (a) RGB image (b) Input disparity map (c) Disparity output from DDP trained with equal weight for RGB and depth loss. The RGB artifacts are evident in (c) through the vertical and horizontal lines representing the wooden planks in the wall (d) Disparity output from DDP trained with lower weight for RGB compared to depth loss. The artifacts disappear in (d).

The RGB based loss helps to resolve the issue of blurring observed around edges near object boundary. However, putting equal weights to disparity L^{disp} and RGB L^{RGB} components of the total loss leads to RGB based artifacts appearing in the disparity image and so in depth output images as well. In particular, these artifacts are due to edges within objects and not at boundary.

For example in Figure 4 the walls of the house is one surface and should have smooth depth maps. However, the DDP network trained on RGBD data generates vertical artifacts in the depth images. These artifacts appear due to availability of vertical wooden planks in the RGB image.

Warping-based loss. To solve the artifact problem, we propose to include a warping loss. Before defining the warping loss, let us first define warping function T_i^j . Given the camera poses C_i and C_j of the views i and j , the function T_i^j warps view i to neighboring view j .

The current view j is the view for which we are trying to generate denoised output z^{out} . We first find top N neighboring views of the current view j . These neighboring views are generated using the method described in MVSNet paper [47]. Let i denote one of these N views and let W_i^j be the warped image from view i to j . Let D_j^{out} be the predicted depth (inverted z_j^{out}) for the j^{th} view and I_i^{in} is the input RGB for the i^{th} view, then the warped image is $W_i^j = T_i^j(D_j^{out}, I_i^{in}; C_i, C_j)$. Further, we also use bilinear interpolation to remove holes in the warped result.

Dataset	SGM	SGM+DDP(Ours)
Ignatius(68 images)	46.20	46.55
Ignatius(34 images)	43.51	43.51
Ignatius(17 images)	31.41	31.63
Ignatius(9 images)	26.79	27.47

(a) We compare the accuracy of DDP on datasets of different sizes. As the number of images become smaller, the holes increase and so we get the most relative performance gain at number of images=9.

Now given I_j^{in} , the input RGB for the j^{th} view we can compute warping loss as:

$$L_{ij}^{warp} = \lambda_w L^{ss}(I_j^{in}, W_i^j) + (1 - \lambda_w) L^1(I_j^{in}, W_i^j). \quad (5)$$

When there are multiple neighboring views, the loss is averaged over them as $L_j^{warp} = \frac{1}{N} \sum_{i=1}^N L_{ij}^{warp}$.

Warping loss not only resolves the issue of artifacts appearing around edges within objects, we observe it helps to improve disparity (and depth values) in other regions as well. Thus, the warping term improves overall precision.

Importance of each loss terms have been demonstrated in the experiment section 4.

Optimization. All three losses that we use are differentiable with respect to the network parameters and so the network is optimized using standard backpropagation.

4. Experiments

We evaluate the effectiveness of the presented approach on multi-view reconstruction task. We demonstrate the qualitative and quantitative improvement on five sequences from the Tanks and Temples dataset (TnT dataset) [23]. These sequences include Ignatius, Caterpillar, Truck, Meetingroom and Barn.

Implementation. In this work, we applied the deep depth prior on a sequence of depth images. In all our experiments, the base network is primarily an encoder-decoder based UNet architecture [31]. The UNet encoder consists of 5 convolution blocks each consisting of 32, 64, 128, 256, and 512 channels. Each convolution operation uses 3x3 kernels. Further, we have also conducted experiments using skip network [42]. Input noise to the network is of size $m \times n \times 16$ where m and n are the dimensions of the input depth images. Training is performed using Adam optimizer. Initial learning rate is set to 0.00005, that is reduced by a factor of 0.01 after 12000 and 15000 epochs. The model trained for 16000 epochs. Hyper-parameters of the loss function are set through searching on a small subset from the TnT dataset.

The depth images are fused using fusibile approach [11] to reconstruct the final 3D point cloud. Fusibile has certain hyperparameters that determine the precision and recall values for the resultant point cloud. These parameters include

Network+Loss	P	R	F
UNet+D	32.33	35.50	33.84
UNet+RGBD	38.50	38.73	38.62
UNet+RGBD+warping	42.83	49.75	46.03
SkipNet+RGBD+warping	42.81	49.77	46.03

(b) The results of comparing the DDP output using disparity, RGBD and warping loss and using UNet or SkipNet as the network are shown here, P:Precision, R:Recall, F:F-Score.

the disparity threshold and the number of consistent views. More details about fusibile and loss hyper-parameters are provided in the supplementary material.

4.1. Quantitative results

Baseline. Our primary comparison is with popular semi-global matching method (SGM) [18] for depth image estimation. SGM is an optimization based method that does not require any training data. We also compare with state-of-the-art learning based MVSNet method [47]. Further, it should be noted that our approach is orthogonal to the depth estimation method, i.e. it could be used as a post process to improve depth maps from any source.

Metric. Reconstructed point clouds are compared to the ground truth point cloud to give us scores on all 5 sequences in the TnT dataset [23]. These scores are computed using the benchmarking code provided by the TnT dataset which return the precision ($P = \frac{TP}{TP+FP}$), recall ($R = \frac{TP}{TP+FN}$) and f-score ($F = 2 \cdot \frac{PR}{P+R}$) values for each scene given the reconstructed point cloud model and a file containing estimated camera poses used for that reconstruction. Here, TP , FP and FN are true positives, false positives and false negatives respectively. For each of the sequences they also fix the point where precision and recall are reported given the precision-recall curve.

Ablation studies We conduct a series of experiments on the Ignatius dataset to study impact of each parameter and component of the proposed method. We first study the effect of number of depth images on final reconstruction. For this purpose, we skip a constant number of images in the dataset. For example, a skip size of two suggests that only every second image is available for reconstruction. It essentially reduces the data size to half. Such reduction in the data size increases the number of holes on the SGM-based reconstruction method. Same reduced data size is used for the baseline and our approach. We also conducted experiments with skip values of four, eight and sixteen.

Table 1a provides details about the impact of this skip size on relative improvement. It can be observed that at skip sizes of 2, 8 and 16, we see an improvement of 0.35, 0.22, and 0.68 percentage point of relative improvement in F-measures over the baseline respectively. It suggests that

Method	N	C	disparity threshold	SGM			DDP(Ours)			SGM+DDP(Ours)		
				P	R	F	P	R	F	P	R	F
Ignatius	68	4	1.0	43.97	48.68	46.20	42.83	49.75	46.03	43.54	50.01	46.55
Ignatius	17	1	2.0	30.17	32.76	31.41	28.80	34.09	31.23	29.32	34.33	31.63
Barn	180	2	0.5	23.34	27.81	25.38	23.04	27.61	25.12	22.78	29.26	25.61
Barn	45	1	4.0	19.06	21.43	20.18	18.38	21.27	19.72	18.10	22.79	20.18
Truck	99	4	1.0	35.76	38.80	37.22	34.30	41.10	37.39	34.54	41.36	37.64
Truck	25	1	2.0	29.44	33.81	31.48	27.93	36.11	31.50	27.69	36.66	31.55
Caterpillar	156	4	1.0	24.92	41.47	31.13	23.80	42.56	30.53	23.96	42.93	30.75
Caterpillar	39	1	2.0	17.28	36.54	23.46	15.89	37.00	22.23	16.21	37.89	22.71
Meetingroom	152	4	1.0	27.51	13.43	18.05	25.39	14.86	18.75	25.24	15.24	19.01
Meetingroom	38	1	4.0	17.80	9.03	11.98	16.08	10.03	12.36	15.68	10.72	12.73

Table 2: Quantitative results comparing 5 sequences for SGM based depths, depths from DDP applied on SGM outputs and also combining the DDP and SGM depths. We combine by replacing the depth values in the holes of SGM depth with DDP depth. Here N: number of images in sequence, C: number of consistent views, P: precision, R:recall, F:f-score.

at higher skip sizes, our approach provides necessarily prior information to fill holes. It should be noted that we have not included experiments with skip size of one. Running fusible on all of the Ignatius images produces dense reconstruction without holes. Running DDP on this dense reconstruction has no effect, and so we have not included results with skip size of one in the table.

Next we show the advantage of using RGBD and warping loss over disparity loss only. Since longer DIP runs on disparity images can return the holes in the result, we run both depth and warping loss based networks for 6000 epochs only instead of 16000. The results are in Table 1b.

Table 1b shows the benefit of photoconsistency based warping loss. We observe a relative improvement of 7.41% point in F-measure after incorporation of the warping loss.

Finally, we also conducted experiments with Skip-Net [42] to show impact of using network different from UNet in Table 1b. They give comparable results and we chose to use UNet since it is a standard commonly used network.

Comparison to prior work. Quantitative comparison with the SGM baseline on the five TnT dataset is shown in the Table 2. The DDP (Ours) column shows the results of using DDP approach to improve SGM depth maps as input. The table includes the precision, recall and f-scores on each dataset with sub-sampled number of images done using the technique described in the Ablation Studies. We observe improvement in recall values of the presented approach over the SGM-method. It suggests the method helps in hole filling. Next we also combine DDP depth maps with SGM depth maps, keeping the SGM values everywhere where there are no holes and replace the holes with DDP depth values. We will refer to this as SGM+DDP(Ours) in Table 2. This leads to better results in 4 of the 5 sequences. Overall SGM+DDP(Ours) helps to improve recall by 1.74 percentage points and f-score by 0.19 percentage points. In

Dataset	SGM+DDP(Ours)			MVSNet		
	P	R	F	P	R	F
Ignatius	43.5	50.0	46.6	37.2	63.0	46.8
Barn	18.1	22.8	20.2	19.1	18.8	18.9
Truck	34.5	41.4	37.6	29.1	51.1	37.1
Caterpillar	16.2	37.9	22.7	25.2	32.9	28.5
MR	25.3	15.2	19.0	18.1	11.9	14.4

Table 3: Results comparing our output applied on SGM depth to MVSNet depth images. P:precision, R:recall and F:f-score. We have applied our results on 5 TnT training datasets. MR: Meetingroom sequence.

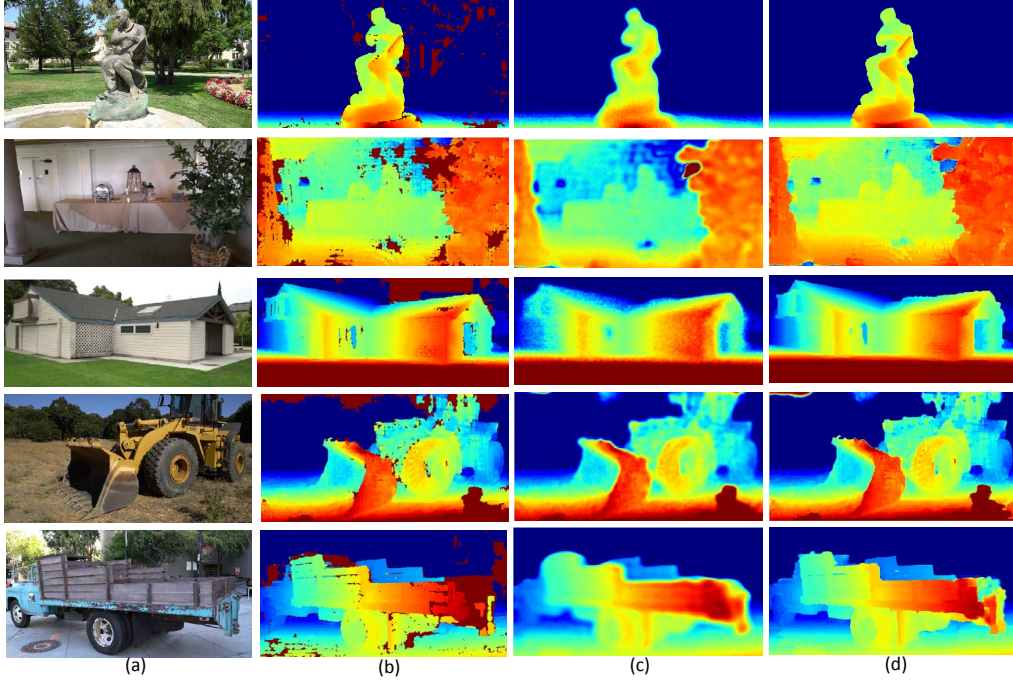
particular, we see a significant improvement of 1.75 in recall and 0.85 in f-score on the MeetingRoom sequence.

Table 3 compares precision, recall and f-scores of SGM+DDP (Ours) method with that of the learning based MVSNet baseline. It is based on applying DDP on SGM depth and not MVSNet depth which means our technique is not learning dependent whereas MVSNet is. Our approach achieves an improvement of 0.1 percentage points for f-score over the MVSNet method. We did not apply DDP on MVSNet depth because depth outputs from MVSNet method do not contain any holes. We can use their probability map which shows confidence of depth prediction to create holes by removing depth at places with confidence below a certain threshold. We provide these experiments in the Supplementary material.

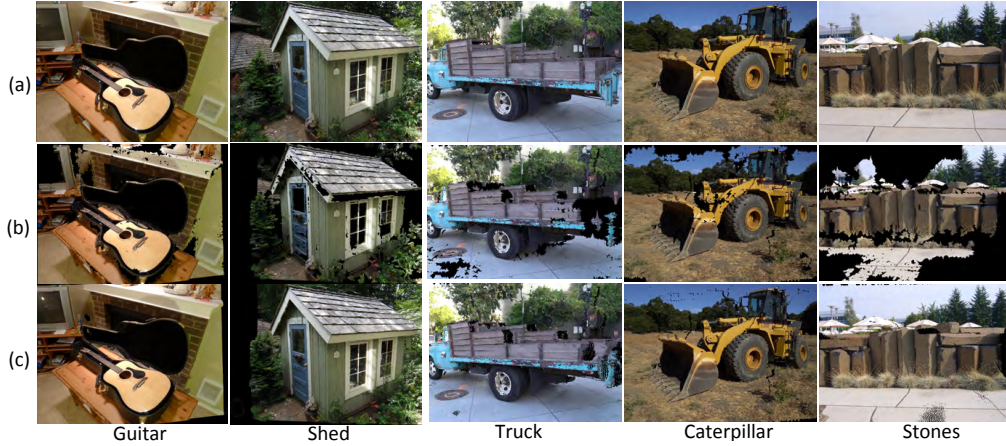
4.2. Qualitative results

Next we provide visual results on TnT dataset to highlight the impact of our approach in achieving high quality reconstruction. We also show outputs on six of our own recordings - Guitar, Shed, RedCouch, Desk, Stones, Van.

In Fig. 5a, we show output disparity images at 500 (column c) and 16000 (column d) epochs of the proposed DDP



(a) (a) Input RGB and (b) input depth images for Ignatius, Meeting Room, Barn, Caterpillar and Truck and predicted depth at epochs (c) 500 (d) 16000.



(b) (a) Original Image from a neighboring view point (b) Novel view synthesized from the same camera view point using the original SGM depth (c) Novel view synthesis from the same camera view point using DDP depth. The holes that appear in (b) gets filled in (c).

approach on five TnT sequences. Note that the holes in the input disparity images (marked as dark red in column b) are filled in the output images (c, d). Further, qualitative improvement can be observed across epochs on comparing visual outputs. For example, disparity of the background wall in second row image is more consistent at 16000 epochs than at 500 epochs.

To better understand the quality of the depth images generated by the proposed method, we warp RGB images using the original and the proposed DDP generated depth im-

ages for Guitar, Shed, Truck, Caterpillar and Stones. The warped RGB images are shown in the Fig. 5b. Holes can be observed in the RGB images warped using original depth maps for example along the smooth reflective side surface of the guitar, the roof of the Shed, some parts of the truck and caterpillar and along the base of the Stone Wall. However, RGB images warped using our depth images removes large portions of these holes, and are smooth.

Finally we also show some reconstructed point clouds in Figure 6. The first column is one of the input RGB im-

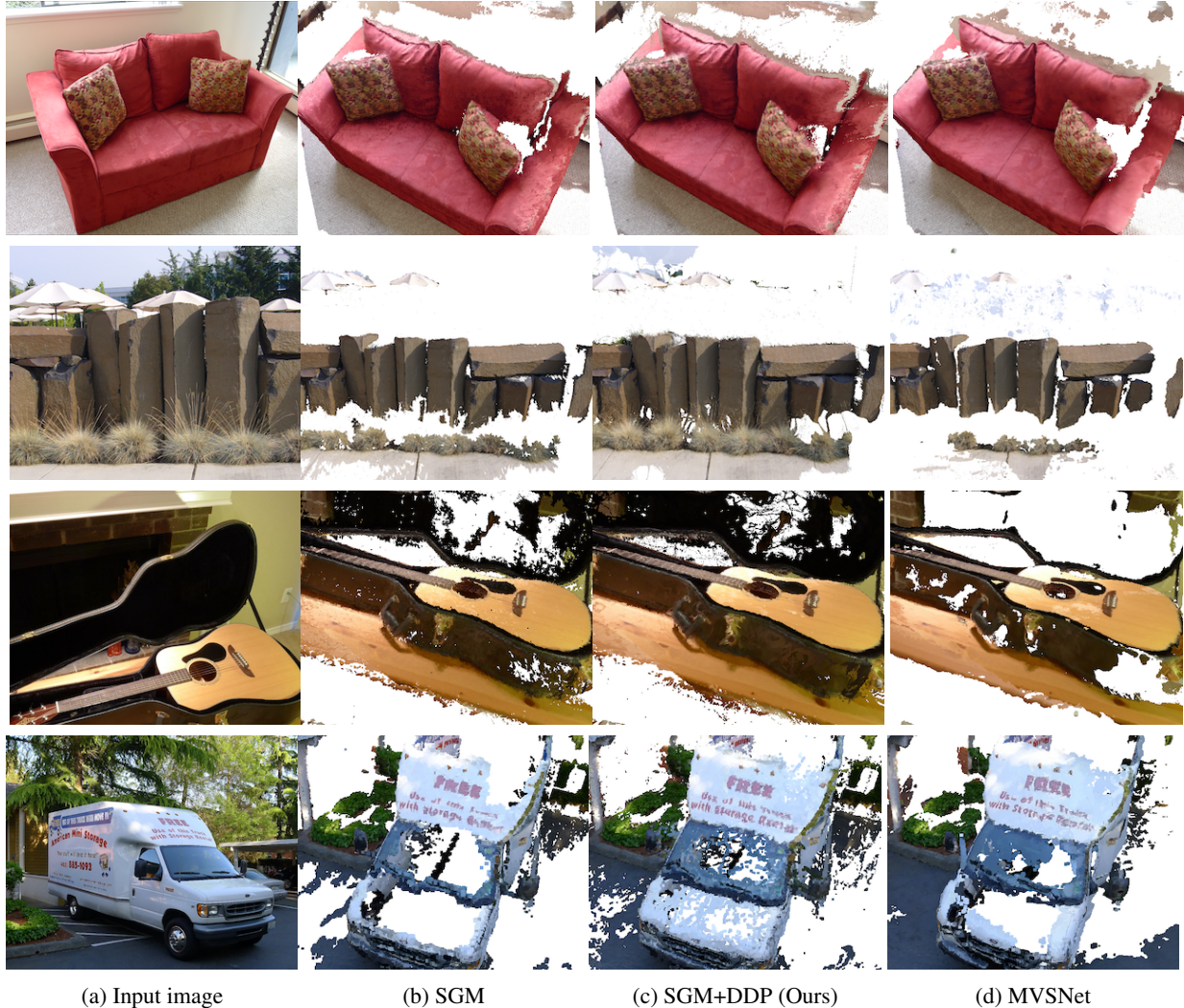


Figure 6: (a) Input RGB image and reconstructed pointcloud from (b) SGM (c) DDP (Ours) and (d) MVSNet depth images for RedCouch, Stones, Guitar and Van. Our reconstructions are more complete.

ages used for the reconstruction, second column is the reconstruction from the original SGM output, the third one is the reconstruction of our results applied on SGM outputs and the fourth column is the reconstructed result from MVSNet.

We used RedCouch, Stones, Guitar and Van for visualization. The number of views used for these reconstructions are small (~ 10). We chose these datasets to show specific ways in which our reconstructions improve on the original SGM and even MVSNet outputs. As we can see from our results, there are a lot less holes in the reconstructions computed from our depth maps compared to original SGM and MVSNet. For example from the top view of the RedCouch in the first row, we can see the relatively obscure region behind the pillow. DDP is successfully fills up a big portion of this hole. Next the base of the Stone Wall in the second row also gets filled. Finally the reflective surfaces of the guitar in

the third row and the van in the fourth row gets completely or at least partially full depending on how big the original hole was.

5. Conclusions

We have presented an approach to reconstruct depth image from incomplete depth image and a color image taken from the same viewpoint. We leverage the recently proposed idea of utilizing neural network as a prior for natural color image, and introduced three new loss terms that reconstruct clean and complete depth image. Extensive qualitative and quantitative experiments on sequences from the Tanks and Temples dataset demonstrated the impact of improved depth images generated by the presented method.

One important future extension includes improving the speed of the method. Further, the presented method could benefit from deeper understanding of the convergence properties of the method.

References

- [1] Henrik Aanæs, Rasmus Ramsbøl Jensen, George Vogiatzis, Engin Tola, and Anders Bjarholm Dahl. Large-scale data for multiple-view stereopsis. *International Journal of Computer Vision*, pages 1–16, 2016. 2
- [2] Christian Banz, Holger Blume, and Peter Pirsch. Real-time semi-global matching disparity estimation on the gpu. In *2011 IEEE International Conference on Computer Vision Workshops (ICCV Workshops)*, pages 514–521. IEEE, 2011. 2
- [3] Jonathan T Barron and Ben Poole. The fast bilateral solver. In *European Conference on Computer Vision*, pages 617–632. Springer, 2016. 3
- [4] Michael Bleyer, Christoph Rhemann, and Carsten Rother. Patchmatch stereo-stereo matching with slanted support windows. In *Bmvc*, volume 11, pages 1–11, 2011. 2
- [5] Michael Bleyer, Carsten Rother, Pushmeet Kohli, Daniel Scharstein, and Sudipta Sinha. Object stereojoint stereo matching and object segmentation. In *CVPR 2011*, pages 3081–3088. IEEE, 2011. 1, 2
- [6] Jia-Ren Chang and Yong-Sheng Chen. Pyramid stereo matching network. In *Proceedings of the IEEE Conference on Computer Vision and Pattern Recognition*, pages 5410–5418, 2018. 2
- [7] Zhuoyuan Chen, Xun Sun, Liang Wang, Yinan Yu, and Chang Huang. A deep visual correspondence embedding model for stereo matching costs. In *Proceedings of the IEEE International Conference on Computer Vision*, pages 972–980, 2015. 2
- [8] Zezhou Cheng, Matheus Gadelha, Subhransu Maji, and Daniel Sheldon. A bayesian perspective on the deep image prior. In *CVPR*, pages 5443–5451, 2019. 3
- [9] Yasutaka Furukawa, Brian Curless, Steven M Seitz, and Richard Szeliski. Towards internet-scale multi-view stereo. In *2010 IEEE computer society conference on computer vision and pattern recognition*, pages 1434–1441. IEEE, 2010. 1
- [10] S. Galliani, K. Lasinger, and K. Schindler. Massively parallel multiview stereopsis by surface normal diffusion. In *2015 IEEE International Conference on Computer Vision (ICCV)*, pages 873–881, Dec 2015. 1, 2
- [11] Silvano Galliani, Katrin Lasinger, and Konrad Schindler. Massively parallel multiview stereopsis by surface normal diffusion. In *Proceedings of the IEEE International Conference on Computer Vision*, pages 873–881, 2015. 5
- [12] Yossi Gandelsman, Assaf Shocher, and Michal Irani. ”double-dip”: Unsupervised image decomposition via coupled deep-image-priors. In *CVPR*, 2019. 1, 3
- [13] Stefan K Gehrig, Felix Eberli, and Thomas Meyer. A real-time low-power stereo vision engine using semi-global matching. In *International Conference on Computer Vision Systems*, pages 134–143. Springer, 2009. 2
- [14] Andreas Geiger, Philip Lenz, Christoph Stiller, and Raquel Urtasun. Vision meets robotics: The kitti dataset. *The International Journal of Robotics Research*, 32(11):1231–1237, 2013. 2
- [15] Michael Goesele, Noah Snavely, Brian Curless, Hugues Hoppe, and Steven M Seitz. Multi-view stereo for community photo collections. In *2007 IEEE 11th International Conference on Computer Vision*, pages 1–8. IEEE, 2007. 1
- [16] Norbert Haala and Mathias Rothermel. Dense multi-stereo matching for high quality digital elevation models. *Photogrammetrie-Fernerkundung-Geoinformation*, 2012(4):331–343, 2012. 1, 2
- [17] Philipp Heise, Sebastian Klose, Brian Jensen, and Alois Knoll. Pm-huber: Patchmatch with huber regularization for stereo matching. In *Proceedings of the IEEE International Conference on Computer Vision*, pages 2360–2367, 2013. 2
- [18] Heiko Hirschmüller. Stereo processing by semiglobal matching and mutual information. *IEEE Transactions on pattern analysis and machine intelligence*, 30(2):328–341, 2007. 1, 2, 5
- [19] Po-Han Huang, Kevin Matzen, Johannes Kopf, Narendra Ahuja, and Jia-Bin Huang. Deepmvs: Learning multi-view stereopsis. In *Proceedings of the IEEE Conference on Computer Vision and Pattern Recognition*, pages 2821–2830, 2018. 1, 2
- [20] Mengqi Ji, Juergen Gall, Haitian Zheng, Yebin Liu, and Lu Fang. Surfacenet: An end-to-end 3d neural network for multiview stereopsis. In *Proceedings of the IEEE Conference on Computer Vision and Pattern Recognition*, pages 2307–2315, 2017. 1, 2
- [21] Alex Kendall, Hayk Martirosyan, Saumitro Dasgupta, Peter Henry, Ryan Kennedy, Abraham Bachrach, and Adam Bry. End-to-end learning of geometry and context for deep stereo regression. In *Proceedings of the IEEE International Conference on Computer Vision*, pages 66–75, 2017. 1, 2
- [22] Arno Knapitsch, Jaesik Park, Qian-Yi Zhou, and Vladlen Koltun. Tanks and temples: Benchmarking large-scale scene reconstruction. *ACM Trans. Graph.*, 36(4):78:1–78:13, July 2017. 2
- [23] Arno Knapitsch, Jaesik Park, Qian-Yi Zhou, and Vladlen Koltun. Tanks and temples: Benchmarking large-scale scene reconstruction. *ACM Transactions on Graphics (ToG)*, 36(4):78, 2017. 5
- [24] Patrick Knöbelreiter and Thomas Pock. Learned collaborative stereo refinement. In *German Conference on Pattern Recognition*, pages 3–17. Springer, 2019. 3
- [25] Patrick Knobelreiter, Christian Reinbacher, Alexander Shekhovtsov, and Thomas Pock. End-to-end training of hybrid cnn-crf models for stereo. In *Proceedings of the IEEE Conference on Computer Vision and Pattern Recognition*, pages 2339–2348, 2017. 2
- [26] Jiangbo Lu, Hongsheng Yang, Dongbo Min, and Minh N Do. Patch match filter: Efficient edge-aware filtering meets randomized search for fast correspondence field estimation. In *Proceedings of the IEEE conference on computer vision and pattern recognition*, pages 1854–1861, 2013. 2
- [27] Wenjie Luo, Alexander G Schwing, and Raquel Urtasun. Efficient deep learning for stereo matching. In *Proceedings of the IEEE Conference on Computer Vision and Pattern Recognition*, pages 5695–5703, 2016. 2
- [28] Nikolaus Mayer, Eddy Ilg, Philip Hausser, Philipp Fischer, Daniel Cremers, Alexey Dosovitskiy, and Thomas Brox. A

- large dataset to train convolutional networks for disparity, optical flow, and scene flow estimation. In *Proceedings of the IEEE Conference on Computer Vision and Pattern Recognition*, pages 4040–4048, 2016. 1, 2
- [29] Jiahao Pang, Wenxiu Sun, Jimmy SJ Ren, Chengxi Yang, and Qiong Yan. Cascade residual learning: A two-stage convolutional neural network for stereo matching. In *Proceedings of the IEEE International Conference on Computer Vision*, pages 887–895, 2017. 3
- [30] Zhe Ren, Junchi Yan, Bingbing Ni, Bin Liu, Xiaokang Yang, and Hongyuan Zha. Unsupervised deep learning for optical flow estimation. In *Thirty-First AAAI Conference on Artificial Intelligence*, 2017. 1
- [31] Olaf Ronneberger, Philipp Fischer, and Thomas Brox. U-net: Convolutional networks for biomedical image segmentation. In *International Conference on Medical image computing and computer-assisted intervention*, pages 234–241. Springer, 2015. 5
- [32] Daniel Scharstein, Heiko Hirschmüller, York Kitajima, Greg Krathwohl, Nera Nešić, Xi Wang, and Porter Westling. High-resolution stereo datasets with subpixel-accurate ground truth. In *German conference on pattern recognition*, pages 31–42. Springer, 2014. 2
- [33] Daniel Scharstein, Tatsunori Tani, and Sudipta N. Sinha. Semi-global stereo matching with surface orientation priors. *2017 International Conference on 3D Vision (3DV)*, pages 215–224, 2017. 2
- [34] Johannes Lutz Schönberger, Enliang Zheng, Marc Pollefeys, and Jan-Michael Frahm. Pixelwise view selection for unstructured multi-view stereo. In *European Conference on Computer Vision (ECCV)*, 2016. 1, 2
- [35] Thomas Schops, Johannes L. Schönberger, Silvano Galliani, Torsten Sattler, Konrad Schindler, Marc Pollefeys, and Andreas Geiger. A multi-view stereo benchmark with high-resolution images and multi-camera videos. In *Proceedings of the IEEE Conference on Computer Vision and Pattern Recognition*, pages 3260–3269, 2017. 2
- [36] Akihito Seki and Marc Pollefeys. Sgm-nets: Semi-global matching with neural networks. In *Proceedings of the IEEE Conference on Computer Vision and Pattern Recognition*, pages 231–240, 2017. 2
- [37] Sudipta N Sinha, Daniel Scharstein, and Richard Szeliski. Efficient high-resolution stereo matching using local plane sweeps. In *Proceedings of the IEEE Conference on Computer Vision and Pattern Recognition*, pages 1582–1589, 2014. 2
- [38] Tatsunori Tani and Takanori Maehara. Neural inverse rendering for general reflectance photometric stereo. In *ICML*, 2018. 3
- [39] Tatsunori Tani, Yasuyuki Matsushita, and Takeshi Naemura. Graph cut based continuous stereo matching using locally shared labels. In *Proceedings of the IEEE Conference on Computer Vision and Pattern Recognition*, pages 1613–1620, 2014. 1, 2
- [40] Tatsunori Tani, Yasuyuki Matsushita, Yoichi Sato, and Takeshi Naemura. Continuous 3d label stereo matching using local expansion moves. *IEEE transactions on pattern analysis and machine intelligence*, 40(11):2725–2739, 2017. 1
- [41] Alessio Tonioni, Matteo Poggi, Stefano Mattoccia, and Luigi Di Stefano. Unsupervised adaptation for deep stereo. In *Proceedings of the IEEE International Conference on Computer Vision*, pages 1605–1613, 2017. 1
- [42] Dmitry Ulyanov, Andrea Vedaldi, and Victor Lempitsky. Deep image prior. In *CVPR*, pages 9446–9454, 2018. 1, 3, 5, 6
- [43] Zhou Wang, Alan Bovik, Hamid Sheikh, and Eero Simoncelli. Image quality assessment: From error visibility to structural similarity. In *IEEE transactions on image processing*, page 600612. IEEE, 2004. 4
- [44] Francis Williams, Teseo Schneider, Claudio Silva, Denis Zorin, Joan Bruna, and Daniele Panozzo. Deep geometric prior for surface reconstruction. In *CVPR*, pages 10130–10139, 2019. 1, 3
- [45] Oliver Woodford, Philip Torr, Ian Reid, and Andrew Fitzgibbon. Global stereo reconstruction under second-order smoothness priors. *IEEE transactions on pattern analysis and machine intelligence*, 31(12):2115–2128, 2009. 1, 2
- [46] Youze Xue, Jiansheng Chen, Weitao Wan, Yiqing Huang, Cheng Yu, Tianpeng Li, and Jiayu Bao. Mvsrft: Learning multi-view stereo with conditional random fields. In *Proceedings of the IEEE International Conference on Computer Vision*, pages 4312–4321, 2019. 2
- [47] Yao Yao, Zixin Luo, Shiwei Li, Tian Fang, and Long Quan. Mvsnet: Depth inference for unstructured multi-view stereo. In *Proceedings of the European Conference on Computer Vision (ECCV)*, pages 767–783, 2018. 1, 2, 4, 5
- [48] Jure Zbontar, Yann LeCun, et al. Stereo matching by training a convolutional neural network to compare image patches. *Journal of Machine Learning Research*, 17(1-32):2, 2016. 1, 2
- [49] C. Zhou, H. Zhang, X. Shen, and J. Jia. Unsupervised learning of stereo matching. In *2017 IEEE International Conference on Computer Vision (ICCV)*, pages 1576–1584, Oct 2017. 1, 2